Mechanical Systems and Signal Processing 238 (2025) 113156

Contents lists available at ScienceDirect

Mechanical Systems and Signal Processing

journal homepage: www.elsevier.com/locate/ymssp

Full length article

A compact 3D bandgap multi-material metamaterial design for vibration testing

A. Annessi [a],*, V. Zega [b], P. Chiariotti [c], M. Martarelli [d], P. Castellini [d]

[a] Department of Agricultural, Food and Environmental Sciences, Università Politecnica delle Marche, Via Brecce Bianche 10, Ancona, 60131, Marche, Italy
[b] Department of Civil and Environmental Engineering, Politecnico di Milano, Piazza Leonardo Da Vinci 32, Milan, 20133, Lombardia, Italy
[c] Department of Mechanical Engineering, Politecnico di Milano, Via Privata Giuseppe La Masa 1, Milan, 20156, Lombardia, Italy
[d] Department of Industrial Engineering and Mathematical Sciences, Università Politecnica delle Marche, Via Brecce Bianche 12, Ancona, 60131, Marche, Italy

ARTICLE INFO

Communicated by X. Jing

Keywords:
Metamaterials
Multi-material
Decoupling
Vibration probe
Vibration testing

ABSTRACT

The use of metamaterials is an established approach in the field of vibration isolation, leveraging their exceptional tunability over a vast range of frequencies. A key challenge in designing lattice structures is the trade-off between geometrical compactness and wideness of the bandgap, i.e. the frequency range in which wave propagation is not allowed. A possible solution to reduce the size of the structure while maintaining or improving its vibrational performances, is to incorporate different materials in the metamaterial design. In this paper, we present a compact metamaterial, whose design is driven by a multi-material approach, that exhibits extraordinary properties in terms of wide frequency bandgap and lower frequency threshold. The vibrational performance of the proposed metamaterial is validated both numerically and experimentally for a unit cell with a side length of 3 cm. The results show a bandgap opening frequency of 1257 Hz and a low pass filter behavior in the range 1.25–13.83 kHz. Therefore, the proposed solution represent a significant advancement in the field of periodic structures, as the structure exhibits low frequency isolation performances relative to unit cell compactness. The proposed solution can therefore be used in several applications, such as in compact hand-held vibration probes and dynamic vibration absorbers.

1. Introduction

Nowadays, the interest of the scientific community is increasing on the topic of metamaterials and their wide area of application. Their extreme versatility and adaptability in conjunction with their high performance and tailor-oriented approach are leading to a revolution in the engineering fields. In general, metamaterials are widely known for their unusual properties, typically not available in nature. The main tasks in which metamaterials excel are wave absorption, isolation and manipulation. Starting from electromagnetism and optics to vibration and acoustics, they changed the way material properties could be tailored to a specific purpose [1]. Due to their high performance over a wide frequency range, spanning from Hz [2–4] to hundreds of kHz [5], they are beginning to emerge as valid solutions in a wide variety of engineering applications.

In the field of vibration isolation, various research groups have proposed solutions to problems in different topics. Yao et al. proposed a micro scale metaplate for vibration isolation in Micro-Electro-Mechanical Systems (MEMS) [6,7]. Moreover, they can be

* Corresponding author.
E-mail addresses: a.annessi@staff.univpm.it (A. Annessi), valentina.zega@polimi.it (V. Zega), paolo.chiariotti@polimi.it (P. Chiariotti), m.martarelli@staff.univpm.it (M. Martarelli), p.castellini@staff.univpm.it (P. Castellini).

https://doi.org/10.1016/j.ymssp.2025.113156
Received 6 May 2025; Received in revised form 8 July 2025; Accepted 27 July 2025
Available online 13 August 2025
0888-3270/

used for reducing anchor losses in MEMS [8]. In [9], metamaterials are employed for joint compressive sensing and simultaneously azimuth-distance location. Moving to examples in the macro scale, Yu et al. [10] proposed a load-bearing support design with integrated vibration-isolation embedding metamaterial absorbers for vibration and noise reduction in power units. Sangiuliano et al. exploit a metal 3D printed resonant metamaterial to reduce structure-born low frequency vibration related to acoustic modes of tyres [11]. Polymer sheets with embedded local resonant systems have been proposed as a flexible and lightweight solution in vibration absorption due to ease of production [12]. Metaconcrete made by single and double mass resonators can be installed in buildings to trap wave energy from shock and vibrations, to reduce the stress in mortar when subjected to dynamic loading [13,14]. Mir et al. proposed a MetaWall for sound insulation and energy harvesting as an alternative for traditional roadside noise barriers [15]. Muhammad et al. proposed an attenuation solution for bearing induced vibration that uses a metahousing consisting of a dissipative elastic metamaterial and exploiting resonant units mismatch to broaden the metamaterial working range [16]. Liu et al. proposed a tunable multi-functional metamaterial sandwich panel that can achieve load-bearing, energy absorption, and low-frequency vibration isolation properties in conjunction [17]. Regarding acoustics applications [18], metamaterials are engineered to be embedded in resonant panels to reduce structure-born noise [19–24].

The design strategy of metamaterials mainly aims at maximizing wave isolation performance, i.e. wideness and position of bandgaps in the dispersion diagram, without sacrificing compactness and load-bearing capacity of the structure itself. For this purpose, different approaches have been proposed from homogenization techniques [25,26] to topology optimization [27–29], to deep-learning driven [30,31] and non-linear design methods [32,33], genetic algorithms based optimization [34]. Lattice geometries [35] with hexagonal [36], chiral [37,38] and controllable gyroscopic chiral [39], star-shaped [40–42] and origami-inspired [43] unit cell designs are examples of solutions available in literature so far. Moreover, a strong interest is to be sought into multi-functional and tunable metamaterials [44–49], combining different physical properties, such as wave propagation, acoustics, heat transfer, electrodynamics and magnetism, to optimally tune metastructure characteristics in order to respond to multiple design requirements. In particular, contributions from Wang et al. [50] and Zhao et al. [51] both focused on reaching appropriate low-frequency vibration and impact isolation performance without sacrificing the load-bearing capacity of the structure. The former exploits rotary buckling deformation and overdamping effect using a hyperelastomer embedded in a metal outer frame arranged on a quadrilateral cell structure. The latter consists of a Quasi-Zero-Stiffness (QZS) metastructure which is customized using an optimization design method considering the complex working conditions required in engineering applications.

The concept of Locally Resonant Materials (LRM), firstly introduced by Liu in [52], exploits the introduction of spring–mass systems to obtain wave attenuation with characteristic lattice dimensions smaller than the targeted wavelength. They have been used widely in the world of metamaterials for narrow frequency band isolation and have been used by researches as a starting point to reach higher and broader wave isolation performances. Claeys et al. designed and analyzed a metamaterial plate for acoustic isolation adding bending local resonators in a rectangular core sandwich, allowing good performances through a lightweight structure [53]. The proposed metaplate can be integrated in structural parts, used in harsh environment and easily tailored to specific applications. Built-in local resonators can also be exploited to design metamaterial beams for vibration suppression without sacrificing the load bearing capacity of the beam [54]. Matlack et al. proposed a scalable elastic metastructure for vibration and noise mitigation at low frequencies which exploited the architected lattice geometry to selectively control local resonant modes [55].

In literature, many other strategies to obtain wide frequency bandgaps also in the low frequency range can be found. Meng et al. proposed a rainbow metamaterial that exploits spatially varying resonators to obtain a broader frequency bandgap. Multi-frequency broadband attenuation could be achieved using a non-symmetric configuration of resonators [56]. In [57], a three dimensional truss-lattice structure is proposed for low frequency wave propagation absorption, coupling the Bragg resonance, originated by a body-centered cubic lattice, and a local resonance, established by locally increasing beam diameters. Claeys et al. proposed different combinations of multiple resonators to achieve multiple stopband filters for reducing vibration in a known transmission path, acting on specific targeted frequency zone [58]. In dissipative elastic metamaterials, damping properties of the constituent unit cell can be exploit to merge attenuation region induced by different resonators, obtaining a broaden version with respect to the undamped case [59]. Non-linearity can be also exploited to attenuate vibration over a wider bandgap range compared with linear solutions [60]. Furthermore, the mixing of local resonances with Bragg bandgaps mechanisms allows one to widen the attenuation frequency range [61]. This mechanism, also presented in [62], is called the modes separation method and the operating principle of the metamaterial presented in the current paper is based on it.

Several works concerning the design of metamaterials characterized by wide and low frequency bandgaps, which exploit the mode separation technique, are present in literature. In Table 1 works related with this topic are summarized in a straightforward way, comparing their performances. The bandgap performance is defined as the ratio of the frequency band ($\Delta\omega$) over the central frequency (ω_c) as given in Eq. (1):

$$\frac{\Delta\omega}{\omega_c} = \frac{2(\omega_t - \omega_b)}{\omega_t + \omega_b} \tag{1}$$

where ω_t is the bandgap closing frequency and ω_b is the bandgap opening frequency. The wider the bandgap, the greater the bandgap performance. Percentage in Table 1 is relative to the effective bandgap, which considers the presence of both local resonances and flat bands in the bandgap.

The unit cell size is also given to account for the metamaterial encumbrance. Finally, numerically retrieved attenuation deeps within the bandgap region is given in dB for the sake of completeness. Note that attenuation is strongly dependent on the number of cells and, therefore, strongly varies between the reported solutions.

In this work, starting from the very promising results proposed by D'Alessandro et al. in [78], a metamaterial is designed as a decoupling element for accelerometer probes applied in automatic end-of-line controls for fast and reliable structural testing in the

Table 1
Metamaterials based on mode separation technique and related references.

Reference	Composition type	Bandgap type	$\Delta\omega/\omega_c$	Unit cell size (mm)	Attenuation (dB)	Year
Hou et al. [63]	Single-Material	3D	86%	60	155	2024
Bao et al. [64]	Single-Material	3D	61%	80	85	2024
Yong et al. [65]	Multi-Material	2D	71%	75	50	2024
Gao et al. [66]	Multi-Material	2D	46%	46	220	2023
Zhang et al. [67]	Single-Material	3D	48%	20	73	2023
Yu et al. [41]	Single-Material	3D	143%	25	450	2022
Jiang et al. [68]	Single-Material	3D	161%	30	40	2021
Muhammad et al. [69]	Single-Material	3D	160%	50	250	2021
Fei et al. [70]	Single-Material	3D	83%	60	200	2020
Muhammad et al. [71]	Multi-Material	2D	92%	1	90	2020
D'Alessandro et al. [62]	Single-Material	3D	140%	50	280	2020
Kumar et al. [72]	Single-Material	2D	87%	25	–	2019
Barnhart et al. [59]	Multi-Material	1D	58%	15	20[a]	2019
Zhou et al. [73]	Multi-Material[b]	1D	155%	100	50	2019
Elmadih et al. [74]	Single-Material	3D	68%	30	77[c]	2019
Muhammad et al. [75]	Multi-Material	2D	150%	2500	30	2019
D'Alessandro et al. [76]	Single-Material	3D	135%	50	300	2019
D'Alessandro et al. [77]	Single-Material	3D	64%	50	250	2018
D'Alessandro et al. [78]	Single-Material	3D	159%	50	230	2017
Lu et al. [79]	Multi-Material	3D	100%	10	–	2017
D'Alessandro et al. [80]	Single-Material	3D	132%	50	75	2016
Acar et al. [81]	Single-Material	2D	74%	119	100	2013

[a] A damping of 100% is considered.
[b] Active components are present.
[c] Experimental data.

context of inspection and quality control applications. The accelerometer is mounted on the tip of the probe and pushed against the target surface under test. The handle must be carefully designed in order to allow for constant contact without introducing spurious vibration, thus representing an efficient decoupling element between the operator (human/cobot/robot) and the sensor. In addition, it has to ensure an axial loading direction during the measurement to avoid shear forces acting on the accelerometer. Some prototypes available so far use rubber to eliminate any spurious interfering inputs, but this solution limits the operating frequency range of the sensor. However, hand-held vibration probes embed metrological issues with respect to fixed-installation solutions. Indeed, the stability of the contact between the sensor and the structure under test is crucial to obtain reliable data. This feature cannot be guaranteed in hand-held solutions. Innovative and efficient vibration probe designs are therefore needed to achieve a twofold goal: (i) ensuring stable and effective decoupling between the operator holding the probe and the sensing element in the required frequency range; (ii) guaranteeing stationary contact between the sensor and the target structure. A metastructure exhibiting a wide and low frequency bandgap represents a promising realization of a decoupling element to be used in a hand-held probe for vibration end-of-line testing applications. To satisfy all the requirements of such an application, the metastructure must be indeed small in size and lightweight to guarantee a comfortable handling, must have an adequate strength to ensure proper loading in the axial direction without bending excessively during the measurement, must present a strong attenuation and show a flat transmissibility in the wide frequency range of interest, i.e. from 1 kHz to 10 kHz, to avoid introducing disturbances in the measurement. Differently from the available results summarized in Table 1, in the optimization process here proposed, the maximum axial load that the metamaterial solution can carry without deteriorating its isolation performances, is crucial and will be considered as a strict constraint in the design process. Therefore, a compromise has to be made between having a wider bandgap characterized by a low starting frequency, the unit cell compactness and the load-bearing capability. In particular, the combination of existing metamaterial design with machined steel component or metal dust improve the load-bearing and the vibration isolation performances of metamaterials, both in terms of resonant frequency tuning and increase of the damping behavior of the structure. State-of-the-art metamaterials are engineered to be extremely tunable with a broad spectrum of applications and high isolation properties. Our outcome is tailored to the specific application of vibration decoupling in the case of vibration probes. The proposed design is capable of combining extremely flexible elements with relevant rigid masses without losing structural integrity and resulting in a very compact and lightweight solution [82]. In this paper, we focus on the bulkiness reduction of the unit cell to move towards greater versatility and ease of use for the considered application. The need to reduce the overall dimensions of the metastructure, while maintaining its vibrational performances, can be achieved by exploiting a multimaterial approach. In addition, we focused on structure modularity for metastructure scalability in size. The paper is organized as follows. Section 2 introduces the design of the metamaterial together with a detailed sensitivity analysis of the bandgap. Section 3 presents the static and dynamic analysis of the finite structure through the use of numerical modeling. A prototype of the metastructure is assembled and experimentally evaluated in Section 4 under static and dynamic conditions. In Section 5, the performance of the isolation element, used in a vibration probe configuration, is assessed in a laboratory setup. Finally, Section 6 summarizes the main conclusions.

Table 2
Material properties for fine polyamide PA 2200 for EOSINT P SLS printers.

PA 2200			
Particle dimension	Laser diffraction	60	µm
Density	Laser sinterized	0.9–0.95	g/cm^3
Tensile modulus	DIN EN ISO 527	1700 ± 150	N/mm^2
Shear modulus	DIN EN ISO 527	1240 ± 130	N/mm^2

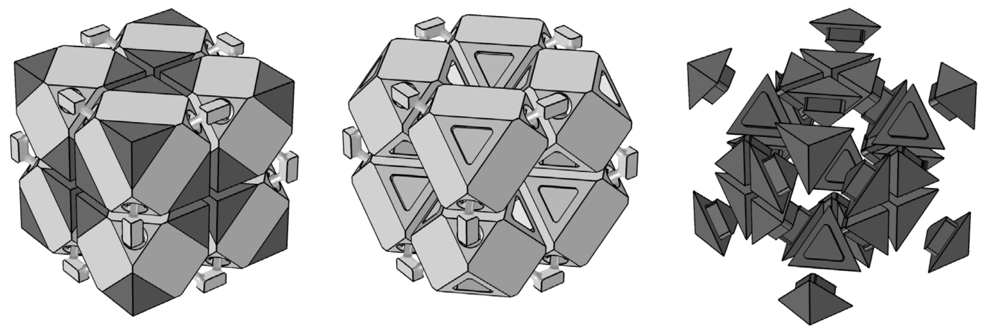

(a) Multimaterial unit cell final assembly. (b) Plastic skeleton. (c) Metal tetrahegonal masses.

Fig. 1. Multi-material unit cell.

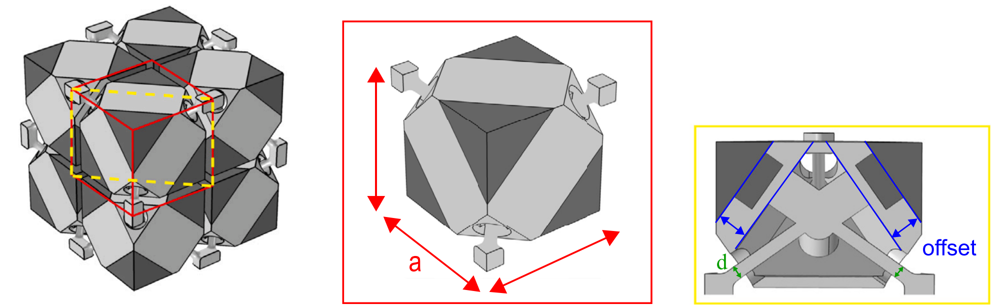

(a) Multimaterial unit cell final assembly. (b) Unit cell size parameter *a*. (c) Steel mass cutting plane referred as *Offset*.

Fig. 2. Unit cell geometric parameters.

2. Unit cell design

The metamaterial geometry here proposed is strongly inspired to the one presented in our previous paper [82]. Here we aim to reduce the bulkiness of the metastructure in conjunction with a bandgap enhancement in terms of frequency performance. The multimaterial approach is then chosen as a promising strategy to achieve the above mentioned goal. The metastructure topology remains unchanged with respect to one published in [82]. Plastic tetrahedral masses, located at the corners, are however replaced with steel ones. Moreover, adequate joints are engineered to connect tetrahedral masses to the metastructure skeleton. Furthermore, slanting beam connections are designed bulkier to be more robust in terms of structural strength and to improve its resistance to fatigue. The resultant multimaterial unit cell is reported in Fig. 1. The full assembly is shown in Fig. 1a, whilst the plastic skeleton and the steel masses are depicted in Fig. 1b and c, respectively. A custom housing is designed to attach the masses to the plastic skeleton.

The Polyamide PA 2200 is chosen for prototyping the internal structure of the system through Additive Manufacturing techniques, e.g. SLS technology. This choice was driven to balance production complexity and system performance. Nominal material properties of PA 2200, which are used for the initial bandgap design, are shown in Table 2. The tensile modulus is equal to 1700 MPa, while a value of 1240 MPa is chosen for the Shear modulus along with a density of 0.9 g/cm^3. The resultant Poisson ratio reads $\nu = E/2G - 1 = 0.31452$, while wave speed can be computed as $v = \sqrt{\frac{E}{\rho}} = 1374$ m/s. The nominal material properties of the steel used for the tetrahedral masses are listed hereafter: tensile modulus is equal to 205 GPa, Poisson ratio ν is equal to 0.28 and the density is equal to 7850 kg/m^3.

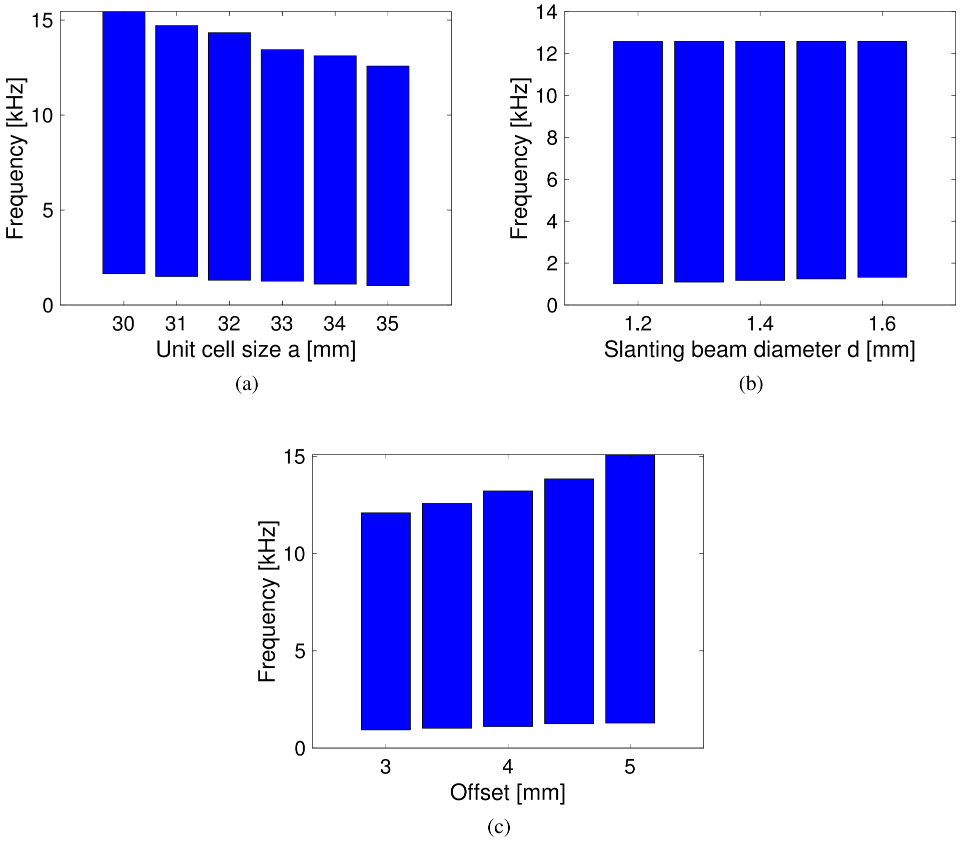

Fig. 3. (a) Bandgap dependence on unit cell size a. The slanting beam diameter is 1.2 mm, while the offset is 3.5 mm. (b) Bandgap dependence on diameter d. The unit cell size is 35 mm, while the offset is 3.5 mm. (c) Bandgap dependence on steel mass offset *offset*. The slanting beam diameter is 1.2 mm, while the unit cell size is 35 mm.

To identify the unit cell geometry parameters that can minimize the encumbrance of the metastructure while maximizing its frequency performances, i.e. moving towards lower frequencies, a sensitivity analysis is carried out. The unit cell size a, the slanting beams diameters d and the steel mass cutting plane *offset* are then chosen as optimization variables (see Fig. 2).

Each parameter has been swept in a range compatible with the 3D-printing technique here employed to fabricate the multimaterial prototype, while keeping the others fixed to the nominal dimensions, i.e. a = 35 mm, d = 1.2 mm and *offset* = 3.5 mm. In particular, the unit cell size a spans from 30 mm to 35 mm, the slanting beam diameter d from 1.2 mm, i.e., the limit of the SLS technology, to 1.6 mm and the *offset* from 3 mm to 4.5 mm. In Fig. 3a, the evolution of the bandgap is reported for different values of a. Note that, by varying a while keeping d and $offset$ constant, we increase the metal mass and the length of the slanting beams. As expected, by increasing the mass and decreasing the stiffness of the slanted beams both the bandgap opening and closing frequencies decrease with the increase of a. To decouple the mass and stiffness effects and identify which is the most relevant contribution, we first analyze the modal shape-functions of the opening and closing modes (see Fig. 4b) and then, we run the parametric study on d and $offset$. From Fig. 4b, it seems that the mass effect is more pronounced than the stiffness one being slanted beams only partially involved in the opening and closing modes. To verify such statement, we plot in Fig. 3b the bandgap evolution under slanted beam diameter variations. As expected, both bandgap opening and closing frequencies are increasing with the slanted beam diameter, i.e. mechanical stiffness, but such effect is much less relevant than the effect evidenced in 3a. Finally, we sweep the $offset$ parameter so to investigate the effect of the mass on the bandgap. Steel is indeed introduced in the geometry on cube corners, cutting and replacing them accordingly to Fig. 1. Thus, the distance of the cutting plane from the center of the cube, called *offset*, defines the base of the steel masses and the relative weights of the two constitutive materials. From Fig. 3c we clearly see the confirmation of the strong influence of the mass on the bandgap width. As expected, by increasing the offset, the metal mass decreases and the frequencies increase.

The need of compactness for easy of usage in the industrial environment led to chose the smallest unit cell size possible for the SLS technology, in this case equal to $a = 30$ mm. Therefore, to compensate the shift versus higher frequencies due to unit cell reduced size, i.e. to lower the bandgap opening frequency while maintaining equal isolation performances, a diameter of $d = 1.2$ mm is chosen, which is the smallest feasible for the manufacturing process. For the same reason, a $offset = 30$ mm is chosen, thus further lowering the bandgap opening frequency. To numerically verify the bandgap properties of the chosen unit cell, a dispersion

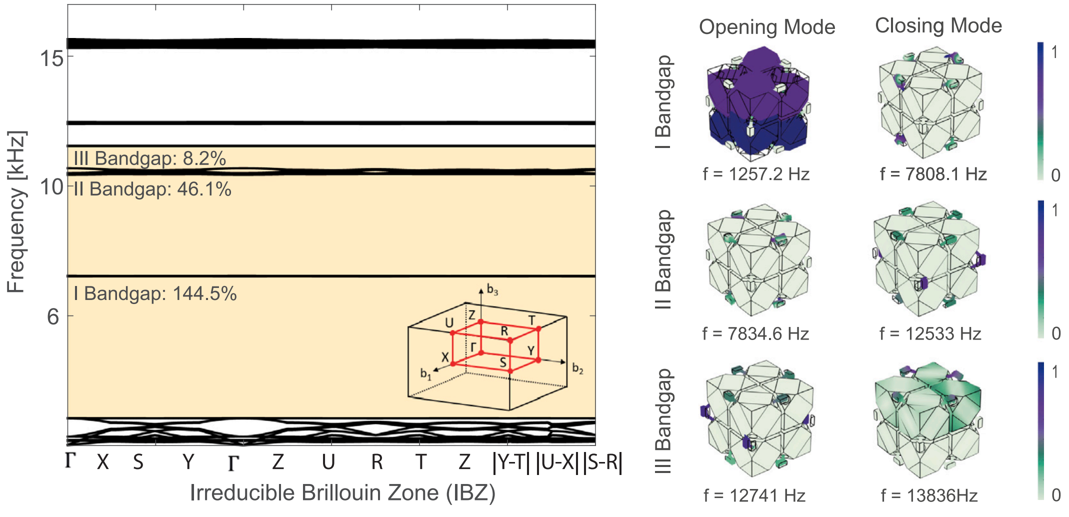

Fig. 4. (a) Numerical dispersion diagram computed in COMSOL Multiphysics©. The considered Irreducible Brillouin Zone (IBZ) is also provided. (b) Modal shape functions of the opening and closing modes of the bandgaps corresponding to the point Z of the IBZ.
The contour of the normalized displacement field is shown in color.

analysis is performed in COMSOL Multiphysics©. Block-Floquet boundary conditions are applied on the four surfaces of the unit cell to simulate the periodic repetition along the three orthogonal directions of the cell in the infinite periodic medium. According to the geometry of the unit cell and to its symmetries, the Irreducible Brillouin Zone (IBZ) shown in the inset of Fig. 4a is chosen for the dispersion analysis [83]. The maximum element size used to mesh geometry is smaller than $\lambda/5$, where λ is the wavelength associated with the highest frequency to be considered (which is equal to 13 836 Hz, refer to Fig. 4 b). From Fig. 4a, it is evident that under the hypothesis of infinite periodic repetition of the proposed unit cell, three wide and low frequency bandgaps are present. The first bandgap opens at 1257.2.1 Hz and closes at 7808.1 Hz, the second covers the range of frequencies from 7834.6 Hz to 12 533 Hz, while the third from 12741 Hz to 13 836 Hz. Moving towards higher frequency, even more bandgaps are present but they are not considered for our purposes. To better investigate the bandgap opening mechanism, in Fig. 4b the modal shape functions of the opening and closing modes for each bandgap are reported together with their dimensional frequencies at the point Z of the IBZ. Similarly to the previous work [82], the opening mode of the first bandgap involves a big modal mass, while the others clearly represent local modes characterized by the deformation of elastic connections as evident from the internal views of the mode shapes reported in the same figure. This proves the employed design strategy and leads to the conclusion that few repetitions of the unit cell are sufficient to obtain a drastic reduction of the wave propagation also in the frequency ranges corresponding to the second and third passbands.

3. Numerical predictions

A transmissibility analysis is carried out in a numerical model using COMSOL Multiphysics© and considering a repetition of three unit cells in the axial direction, obtaining a $1 \times 1 \times 3$ metastructure. In order to be representative of the experimental test, the input signal is provided in terms of acceleration as a sine wave in the z-axis direction applied to the base of the metastructure while the output signal is evaluated in a small circular area on the top surface of one of the cubes from which the geometry is composed, as shown in Fig. 5a. The transmissibility function, which is shown in Eq. (2), is ultimately calculated as the ratio of the output acceleration to the prescribed input acceleration, which is set at $1\ \mathrm{m/s^2}$. To replicate the clamped conditions of the experiments, no displacements along the x- and y-directions are allowed on the bottom surface of the metastructure.

$$T(f) = \frac{A_{out}(f)}{A_{in}(f)} \tag{2}$$

The transmissibility curve is obtained for the Young's Modulus declared by the manufacturer considering no material damping. Moreover, in order to be able to compare numerical results with experimental measurements, the Young's Modulus of PA 2200 is updated to 1350 MPa according to our previous work [84]. The comparison between transmissibility results with no damping are represented as solid lines in Fig. 5b. The theoretical attenuation in the undamped case using the updated Young's Modulus reach a maximum of 360 dB. Lastly, material dissipation is introduced using a complex stiffness in the numerical model to better reproduce the real behavior of the final metastructure. The complex Young's Modulus can be written as a first order Newton model which reads $\overline{E} = E(1 + i\tau\omega)$, where i is the imaginary unit, ω is the circular frequency and $\tau = 3\ \mu\mathrm{s}$. Damping considering a linear dependency on frequency is used to model the material behavior as a first approximation. In this case, the theoretical attenuation

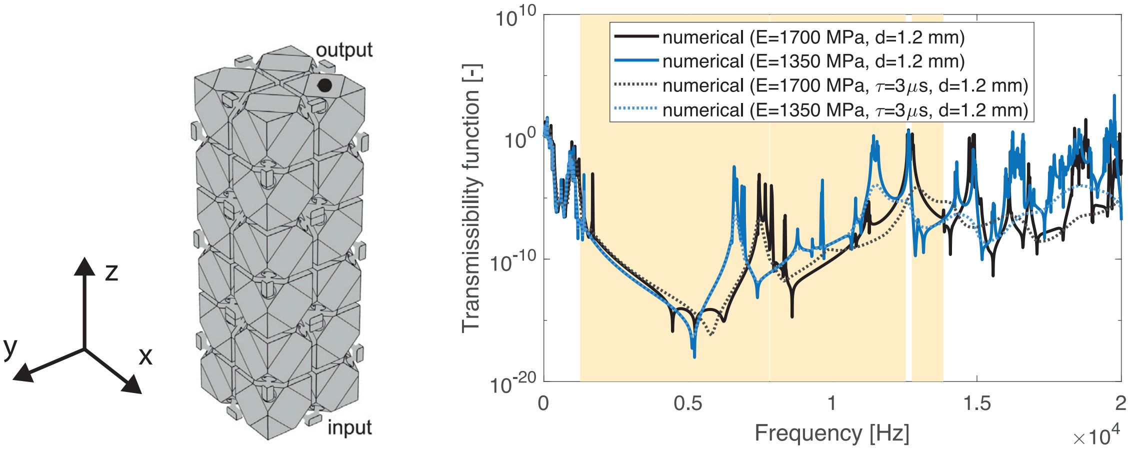

(a) (b)

Fig. 5. Numerical transmissibility computed in COMSOL Multiphysics© reported with theoretical bandgaps computed through the dispersion analysis in yellow for comparison. A schematic view of the 1 × 1x3 multimaterial metastructure is reported for the sake of clarity.

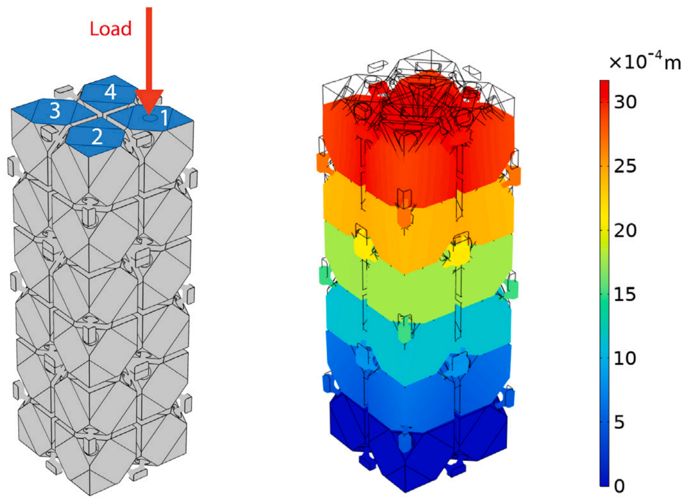

(a) (b)

Fig. 6. (a) Load direction imposed on the top surface of the metastructure (b) Displacement field due to the superposition of gravity load and surface load of 10 N distributed on all four masses.

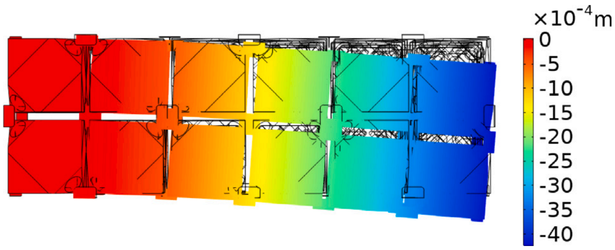

Fig. 7. Gravity load maximum numerical displacement along gravity direction for the multimaterial metastructure.

reach a maximum of 326 dB. The finite nature of the designed metastructure and the boundary conditions imposed at its base result in small variations in the transmissibility function if compared to the opening and closing frequencies of the bandgaps in the dispersion diagram. Considering no material damping in the numerical simulation, passbands exhibiting an amplitude equal to one or bigger are related to big modal masses. In these scenarios, vibration transmission or even amplification is present. On the contrary, passbands exhibiting amplitude reduction of several order of magnitude are associated to low modal masses and local modes of the structure, whom cannot be properly excited by the external forcing applied to the cubes at the metastructure base. All observations are in line with results presented by D'Alessandro et al. [78]. To verify the structural characteristics of the proposed $1 \times 1 \times 3$ metastructure and then its applicability as hand-held vibration probe, we run a static linear analysis in COMSOL Multiphysics©. In particular, we simulated the effect of the self-weight for vertical and horizontal configuration, which are the best and worst in-operation condition for the proposed design. In the former case, the metastructure acts as an axial spring with gravity acting along the z-axis. In the latter case, the metastructure acts as a cantilever beam with gravity acting along the y-axis. The base surface of the metastructure is assumed fixed on all simulations. The metastructure compression due to self-weight in vertical configuration is assessed. The resulting displacement field gave as result a maximum stroke of 0.15 mm along the axial direction. This value is considered small enough to be neglected in future analysis and experimental campaigns. Hereafter, the case of an off-centered compression load distributed on each single sub-area (identified as labeled areas 1, 2, 3, 4 in Fig. 6a) of the top unitcell surface is considered. The load direction is depicted in Fig. 6a and the distributed load is globally equal to 10 N. The load magnitude is chosen to emulate the real application of a hand-held vibration probe, already discussed in [82], in which the static pre-load is typically along the axis of the decoupling element and in the range around 10 N. The worst condition that can occur for the accelerometric probe is to be subjected to an eccentric force leading to off-axes stresses. This condition is emulated in the simulation by applying an off-centered load. In the first case, the load is imposed on a single mass of the top surface (referred as 1 in Fig. 6a), resulting in a maximum displacement of 13.78 mm in the axial direction. In the second case, the same load is applied on two different adjacent masses of the metastructure (referred as 1 and 2 in Fig. 6a), obtaining a maximum stroke of 8.59 mm along the axial direction. Lastly, the load is applied on the whole top surface (referring to top surfaces 1, 2, 3 and 4 in Fig. 6a), resulting in a stoke equal to 3.17 mm which is a reasonable value for practical applications. In this last condition, the displacement field represented in Fig. 6b. The deflection due to the self-weight for the multimaterial metastructure, considered as a cantilever beam, has a maximum bending equal to 4.24 mm, which is in line with the application requirements as hand-held probe. The displacement field for the cantilever case is shown in Fig. 7. Maximum displacements are similar in both single [82] and multi material designs. In fact, they are roughly characterized by the same stiffness and dynamic response.

4. Experimental analysis

A prototype of the metastructure is then manufactured by additive techniques and subsequently assembled manually. The plastic skeleton and the steel masses are manufactured separately and glued together afterwards. The skeleton is realized by Selective Laser Sintering (SLS) technology via an EOS P printer. Tetrahedral masses are made in steel by Bound Metal Deposition (BMD) using a Desktop Metal Studio System.

Each manufacturing process shows different tolerances. The EOS P printer ensures a tolerance of ± 0.2 mm for a dimension up to 50 mm, ± 0.3 mm for a dimension up to 100 mm and 0.3% for dimensions greater than 100 mm. Moreover, component shrinkage due to non-uniform cool-down, which depends on the prototype position on the printing bed, can also be present. On the other side, the Desktop Metal Studio System exhibits tolerances of $\pm 0.8\%$ for parts/features larger than 60 mm and of ± 0.5 mm for part/features smaller than 60 mm. Therefore, the Computer Aided Design (CAD) model has to consider the adequate clearances to make junctions between the plastic skeleton and the metal masses possible. Metal masses junctions are designed 0.1 mm smaller than the site on which they will be mounted on the plastic skeleton sites to account for the process tolerances.

The assembling process for the multimaterial metastructure is shown in Fig. 8. One of the 96 tetrahedral steel masses is shown in Fig. 8a. The first step is to glue the masses on each of the unit-cell plastic skeleton with cyanoacrylate, as shown in Fig. 8b, obtaining the full multi-material unit cell depicted in Fig. 8c. Then, the 3 complete unit cells are attached together in a row producing the final metastructure shown in Fig. 8d.

The mass of the metamaterial and its components is estimated using a weighting scale with an accuracy of 0.01 g. Measurements are taken three times for each component for data consistency. The fully assembled multimaterial metastructure shows a mass equal to 97.45 g. Four metal tetrahedral masses are evaluated independently obtaining an average mass equal to 0.70 g with a standard deviation lower than the scale accuracy. Lastly, three plastic unit cell skeletons are evaluated independently obtaining an average mass equal to 10.41 g with a standard deviation of 0.27 g. Experimental masses are compared to masses retrieved from the material density used in the FEM simulation and the elements volume computed from CAD drawings in Table 3. Despite the geometry modification performed to allow the assembly, the manufactured matastructure is 7% lighter than the numerical model due to uncertainties related to geometry and material properties. Further modifications in the numerical model are then required to be able to reproduce the real behavior of the metastructure.

The first comparison between numerical predictions and experiments is performed by looking at the static behavior of the metastructure. Experiments are performed employing a laser profilometer Wenglor MLSL134 (working distance range 100–500 mm with a Z depth resolution equal to 12.4–160 μm and a X plane resolution equal to 68–246 μm) firmly mounted on a robotic harm. The metastructure axial compression due to self-weight in vertical configuration is not an issue for the application here addressed. Therefore, the measurement campaign is carried out to evaluate the metastructure deflection when considered as a cantilever. The metastructure is then glued to a rigid base by beeswax, as shown in Fig. 9.

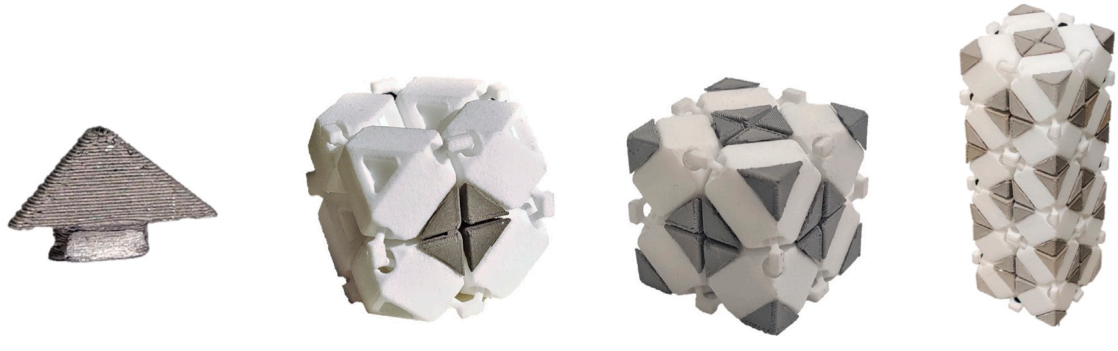

(a) (b) (c) (d)

Fig. 8. Picture of the (a) inner metal mass, (b) unit-cell plastic skeleton with four metal masses mounted, (c) the fully assembled unit-cell and (d) the final metastructure.

Table 3
Experimental versus numerical mass value for the metastructure components.

	Experimental	Simulation	Difference
Tetrahedral steel mass [g]	0.7	0.81	0.11
Plastic skeleton mass [g]	10.41	9.09	1.32
Full assembly mass [g]	97.45	104.57	7.12

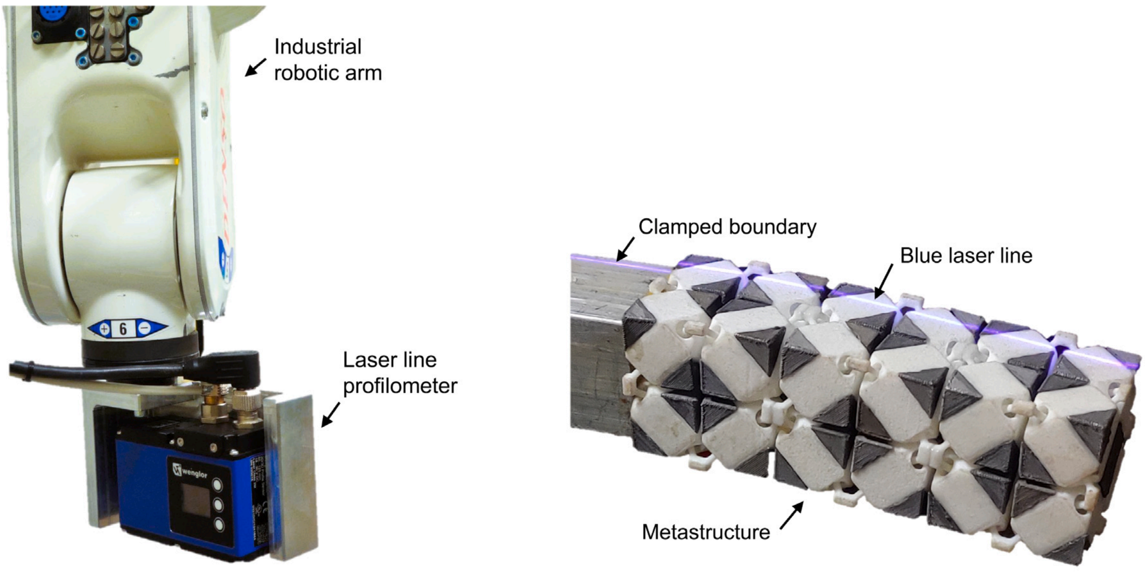

(a) (b)

Fig. 9. Experimental setup for static tests. (a) Laser profilometer and (b) metastructure deformation when employed as a cantilever.

The profile is evaluated on different positions, as the profilometer is moved over the part via the robotic harm in the measurement plan. This scanning operation makes it possible to obtain the metastructure surface scanned on 100 profiles. The data are then cleaned from outliers obtaining the experimental data points from Fig. 11a. Afterwards, points are fitted with a 4-th degree polynomial curve, which gives the best residue distribution as shown in Fig. 11b. Considering the residual in Fig. 11c having a normal distribution, it is possible to evaluate the mean value and the standard deviations, which are respectively equal to 0 mm and 0.07 mm. The curve equation reads $f(x) = -1.321e-07x^4 + 3.663e-05x^3 - 0.003719x^2 + 0.05501x - 0.005754$. The maximum stroke value taken from the experimental campaign is equal to 7.36 mm removing any possible linear trend due to verticality, planarity, and parallelism uncertainty between the reference surface and the profilometer laser blade. As expected, the significant deviation obtained from the numerical analysis, which is equal to 3.12 mm, can be ascribed to the uncertainties of the manufacturing process.

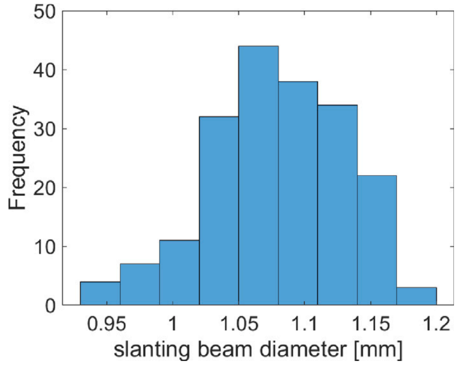

Fig. 10. Histogram of the slanting beam measurement distribution.

Therefore, the diameter of the slanting beams in the skeleton is measured by a centesimal caliper obtaining an average diameter of 1.07 mm along with a standard deviation of 0.05 mm, considering 195 measurements. The histogram of the distribution is shown in Fig. 10. The identified diameter is in line with the declared tolerance for the fabrication process, which is ± 0.2 mm for the specific case. A simulation is carried out using the experimental Young's Modulus, which is the same value used in the numerical section, while varying the slanting beam diameter of the skeleton to cope with the dimensional uncertainty. Considering a slanting beam diameter of 1.1 mm and 1.0 mm, the numerical maximum stroke values are equal to 5.76 mm and 7.79 mm, respectively as shown in Fig. 11a. The deflection retrieved from experimental data fits in between the latter two, confirming the need to account for manufacturing process uncertainties.

Once the static behavior of the proposed metastructure is tested numerically and experimentally, the dynamic response is also investigated in terms of the transmissibility function, verifying the extension of the bandgap and the opening limit of the low frequency. A schematic representation of the experimental setup is shown in 12a. The setup consists of several components. An electro-dynamic shaker (Data Physics V20 - armature resonance around 12 kHz), giving the input signal, on which the manufactured multimaterial metastructure is fixed by means of double-sided adhesive. Two miniaturized single-axis accelerometers (PCB model 352C23), having sensitivity respectively equal to 5.39 mV/g and 5.11 mV/g and characterized by a frequency range from 2 Hz to 10 000 Hz (%5) [85], are attached on the shaker plate and on the top surface of the metastructure to sense the input and output signals. An acquisition and generation system, the Siemens LMS SCADAS mobile, is exploited to generate the excitation signal supplied to the electro-dynamic shaker and acquire both accelerometric signals. The excitation signal, a band-limited white noise in the acquisition frequency range, is provided to the shaker power amplifier (Gearing & Watson Power Amplifier PA 30) which drives the electro-dynamic shaker acting on the lower surface of the metastructure. The bandwidth chosen for the acquisition spans from 0 to 10 kHz, with a frequency resolution of 1.25 Hz. This frequency range allows to acquire data under the optimal sensing range for the accelerometers and to stay away from the shaker resonance, which can cause non-linearity in the response. Each measurement is averaged over 128 acquisitions. The Hanning window is chosen for the accelerometer signals to avoid leakage-related issues.

The experimental transmissibility function is then obtained as the ratio between the output and input accelerations in the frequency domain. A transmissibility value of 1 is associated to no vibration attenuation (the input signal is equal to the output). A value smaller than 1 is referred to an amplitude attenuation, while a value bigger than 1 is referred to an amplitude amplification. Fig. 12b shows the comparison between the experimental results and the numerical predictions, considering the first approximation damping. Moreover, a sensitivity analysis is carried out on the diameter dimension to cope with production uncertainties highlighted previously. The experimental curve in Fig. 12b clearly shows an attenuation of more than two order of magnitude in the experimentally investigated bandgap region spanning from 1257.2 Hz to 10 000 Hz, being the upper frequency limit for the sensors. Moreover, a good agreement between experiments and numerical model is found over the measurement frequency range. In particular, in the range between 4 kHz and 7 kHz, when local modes are predominant, numerical predictions are closely aligned with experiments considering a slanting beam diameter equal to 1 mm. Lastly, attenuation levels obtained in the numerical models are not achievable through experiments due to measurement noise.

5. Operating conditions assessment

Once the static and dynamic behavior of the proposed metastructure is tested, an innovative vibration probe is built and experimentally verified. The scope of this experiment is to test the metastructure in operating conditions, i.e. including all the vibration probe components, on a laboratory setup where the test surface vibration is under control thanks to the presence of a feedback loop.

The innovative vibration probe is composed of the metastructure glued on a threaded rod by means of beeswax. This part is then mounted on a small press for testing. A cross-shaped cross section connection element is manufactured through the Fuse Deposition Molding additive manufacturing technique and then installed between the accelerometer and the metastructure by means of beeswax, which can adapt easily to surface asperities. Adhesive tape can be used an alternative in the case of flatter and smoother

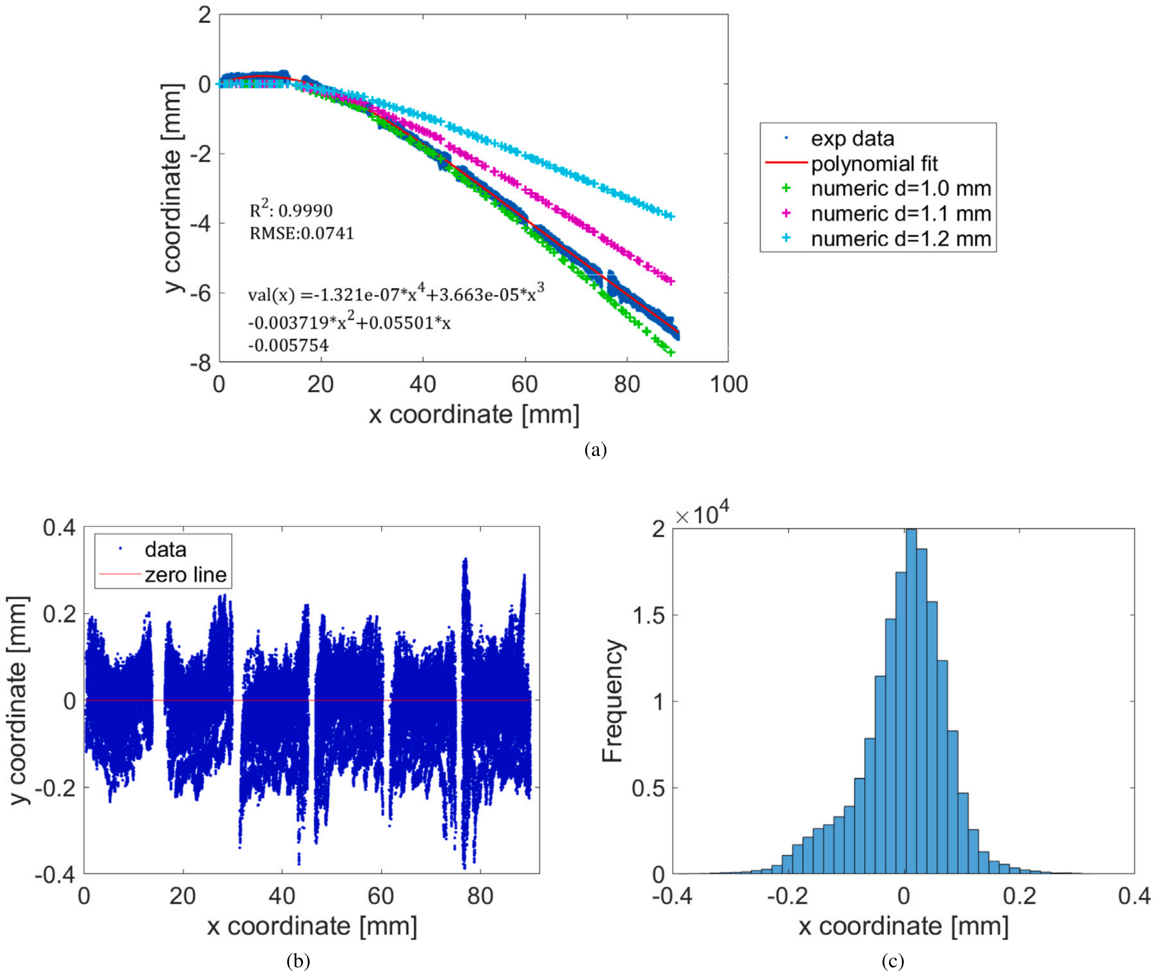

Fig. 11. (a) Laser profilometry raw data fit with a 4-th order polynomial. (b) Residuals. (c) Residuals distribution.

surfaces. Note that both solutions can be also used without compromising the functioning of the component. Lastly, the accelerometer is attached to the connection element through a little layer of beeswax. The design of the connection element installed between the accelerometer and the metastructure is fundamental to avoid unwanted vibrations due to emerging resonances caused by the accelerometer itself or the connection element. In the present realization the cross-shaped connection element, shown in Fig. 13, has indeed a maximum dimension of 16 mm and a thickness of 1 mm, the arms of the cross are 4 mm width.

The vibration probe, once equipped with the accelerometer, is pressed against the surface under test to perform the measurement. The setup is schematically shown in Fig. 14. It consists in the same instrumentation exploited for the transmissibility tests shown in the previous section, the main difference is in the acquisition/generation system which not only allows the acquisition of accelerometers data and the generation of the shaker excitation, but also controls the response of the apparatus, i.e. the probe and the shaker, to avoid dangerous resonances, which could led to instrumentation damage. This feedback control is possible monitoring the response of the two miniaturized accelerometers attached to the metastructure through the connection element (response accelerometer in Fig. 14) and to the shaker plate (control accelerometer in Fig. 14), respectively.

The shaker plate is then excited with a sine sweep in the frequency range of interest, (e.g., for the specific case, spanning from 100 Hz to 10 kHz). To avoid damaging the shaker, a closed-loop on the control acceleration is also exploited. The acceleration is kept constant at a value around 1.6 g. To perform the tests, the metastructure is pushed in different steps against the aluminum plate threaded on the shaker, i.e the preload is varied in terms of displacement, by means of the threaded connection to the press, maintaining contact between the response accelerometer and the surface under test. A laser triangulation system is finally used to measure the metastructure top surface static displacement that provides the preload amplitude through the force–displacement curve.

Experimental data analysis is carried out similarly to transmissibility evaluations presented in Section 4. In this case, making the ratio between the response accelerometer and the control accelerometer signals in the frequency domain, it is possible to evaluate the

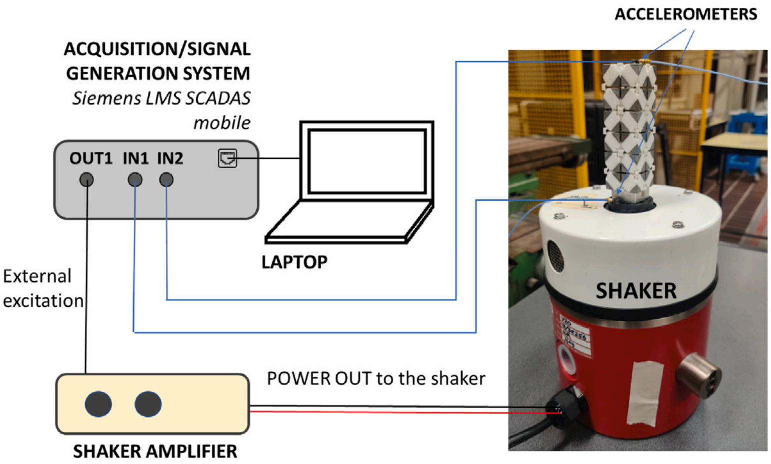

(a)

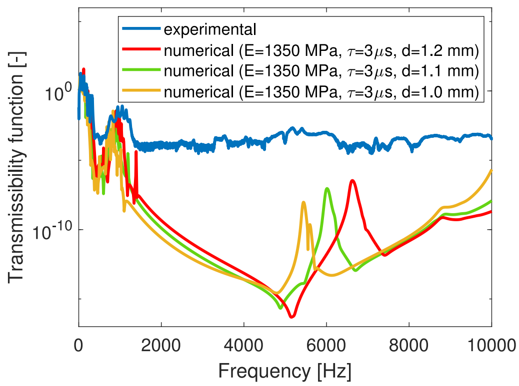

(b)

Fig. 12. (a) Experimental set-up. (b) Transmissibility diagram: comparison between numerical predictions and experiments.

(a) (b)

Fig. 13. (a) Cross-shaped connection element and (b) final installation between the metastructure and the accelerometer by means of beeswax.

goodness of the metamaterial-based probe compared to the accelerometer traditionally installed. This ratio is defined as *Interfering Effect (IE)* and takes into account the intrusiveness of the metastructure on the measurement performance.

To properly evaluate the IE of the system, the excitation feedback control should be taken into account. In fact, the vibration performance of the probe strongly depends on it. The control tends indeed to modulate the excitation such that the system works in a safe manner (avoiding resonances leading to failure). The IE coefficient would be equal to 1 also in presence of a controlled undesired resonance peak. Thus, when assessing the performance of the probe, the control driver data needs to be checked to ensure it does not spoil the results.

Before starting tests, the driver control response is measured in free conditions (i.e. without the metastructure pushing against the shaker plate) and with only the control accelerometer attached. The driver transmissibility is reported in Fig. 15 in agreement with results published in [86]. Therefore, the curve in Fig. 15 will be taken as a reference for the subsequent measurements: a change in amplitude in the driver control curve is an indicator of an approaching resonance that needs to be limited.

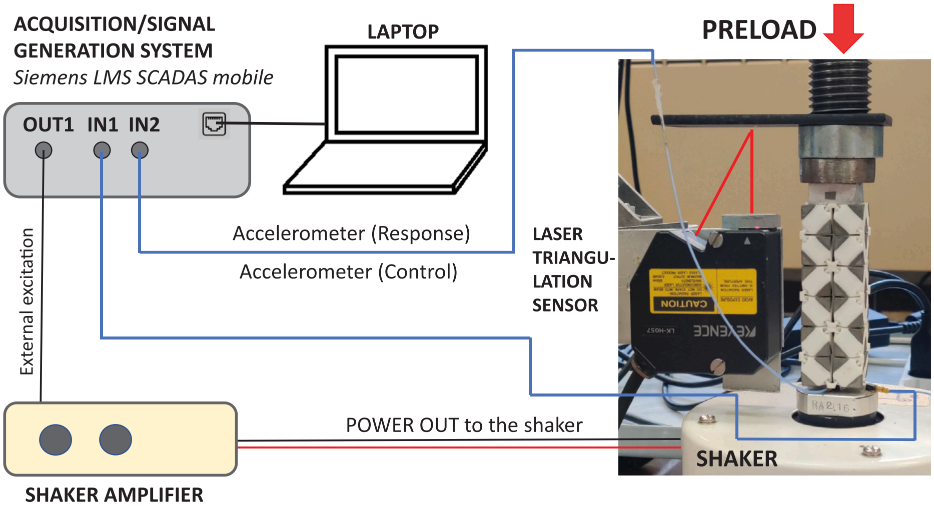

Fig. 14. Schematic view of the experimental set-up employed for the test of the proposed vibration probe in operating conditions.

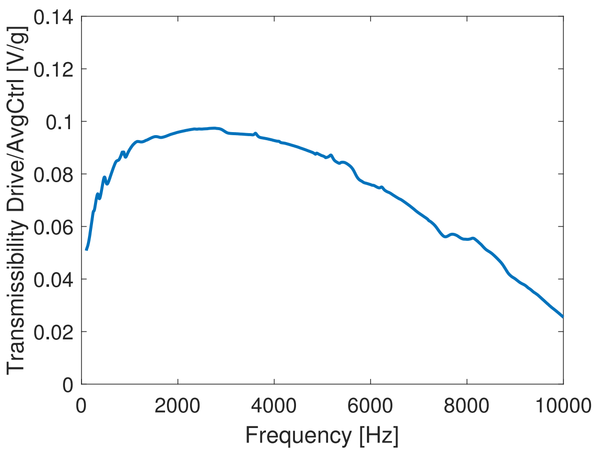

Fig. 15. Driver voltage against average control accelerometer [V/g] measured when only the control accelerometer is attached to the shaker plate and the vibration probe is not installed.

The optimal preload range to be used for the final application is experimentally evaluated. This analysis is crucial in order to guarantee repeatable measurements. If the vibration probe is supported by a robotic arm, the preload can be indeed controlled through a force sensor and kept constant during measurement operations. If, however, the probe is held by hand, it is necessary to determine how the performance of the probe changes with the preload variation due to the operator. Experimental results are compared for different preloads imposed on the metastructure by turning the threaded rod installed in the press. The preload range from the nearly undeformed state, i.e. 0 mm, to a stroke of 6.3 mm, chosen to guarantee linearity in the response and, thus, avoiding buckling phenomena. The incremental step used for the test is not constant due to the low precision of the available threaded rod system. Nevertheless, it allows for properly spanning the full preload range.

The *Maximum Deviation* (MD) index is defined as the mean and the standard deviation of the IE calculated on the frequency band of interest, spanning from 0 Hz to 10 kHz. The mean and the standard deviation are computed respectively as in Eq. (3) and (4), where N is the number of spectral lines.

$$\mu_{MD} = \frac{1}{N}\sum_{i=1}^{N} IE(f(i)) \tag{3}$$

$$\sigma_{MD} = \sqrt{\frac{1}{N}\sum_{i=1}^{N}(IE(f(i)) - \mu_{MD})^2} \tag{4}$$

The MD is chosen to identify the preload that guarantees the best vibrational performance of the metastructure probe. Despite this index has no traditional statistical relevance, it can be employed to estimate the goodness of the measurement performed through

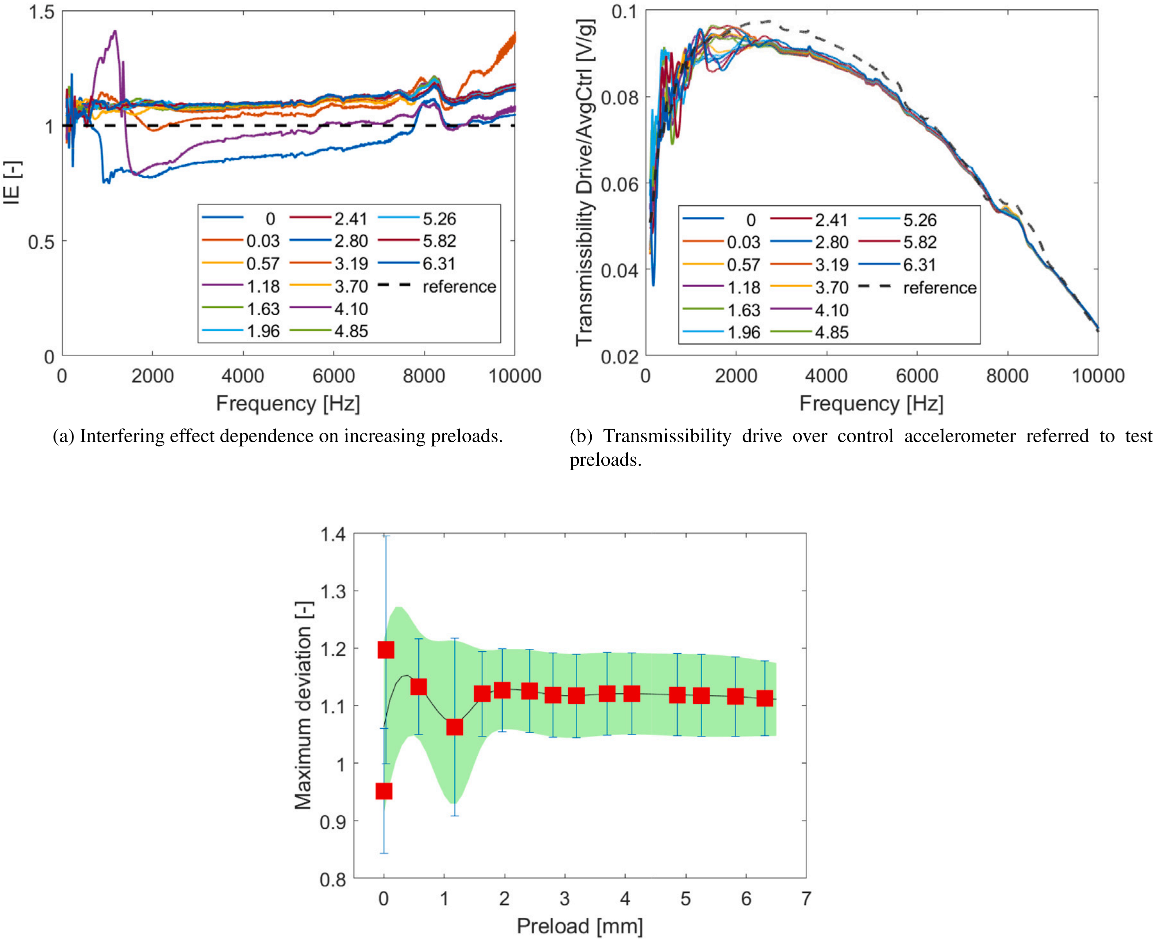

(a) Interfering effect dependence on increasing preloads.

(b) Transmissibility drive over control accelerometer referred to test preloads.

(c) Maximum deviation over test preloads. Mean values are depicted as red squares, whilst standard deviations are represented as error bars.

Fig. 16. Experimental results in operating conditions.

the metastructure vibration probe. The mean value gives indeed an estimation of the deviation from the ideal value of 1, i.e the condition in which the accelerometer pressed with the metastructure on the aluminum plate measures exactly like the one attached with beeswax. The standard deviation gives information about how much the IE fluctuates around the mean value, i.e. how constant the vibration probe performance is. A good solution should be characterized by a mean value approaching one and a low deviation from it. The IE and the drive control curves are shown for each preload value in Fig. 16a and b. Low preloads are clearly associated with a less straight behavior of the IE curve and are characterized by the presence of significant resonances. Increasing preload values, both IE and drive control curves become more stable. The MD is calculated for each preload value in Fig. 16c. Hence, the best preload option can be chosen, given by a displacement of 5.26 mm.

For the sake of completeness, the operating conditions assessment procedure has also been carried out for the single material metamaterial case published in [82]. In this case, the optimal preload equals 6.15 mm.

A typical commercial solution for vibration measurements, i.e. DISCOM vibration probe, is finally considered in comparison with the proposed solution. Its performances were tested in our facility, prior to this work, using a similar close-loop setup with control on the acceleration. The Root Mean Square (RMS) value is used for data comparison and analysis.

Transmissibility curves in operating conditions for both the DISCOM solution and the metastructure discussed in this paper are then compared on the same chart shown in Fig. 17.

In the very low frequency range, the DISCOM vibration probe works better compared to the metastructure one. This is expected since the metastructure is designed to be used in its frequency bandgap, thus above approximately 1500 Hz for the single material version and approximately 1300 Hz for the multi material one. The single material metastructure IE response is nearly constant until 7 kHz. The multi material metastructure version is characterized by an even better response, nearly flat in all the frequency range of interest. Thus, even if in a preliminary design geometry, the single material metastructure already published in [82] and the multi material metastructure proposed in this work seem to be a good solution to be used as a decoupling element for a hand-held vibration probe.

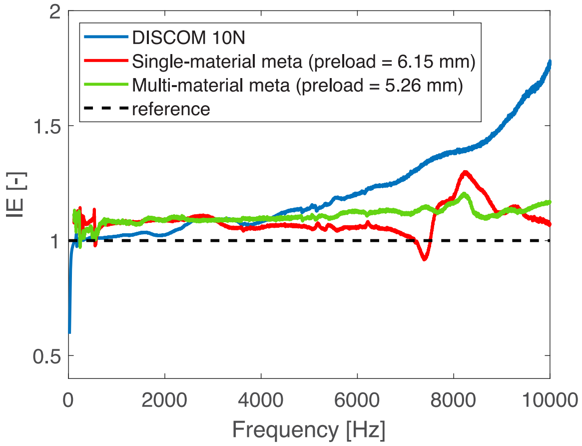

Fig. 17. Experimental Interfering Effect measured on the commercial solution and on the two metastructure probes proposed by the authors.

6. Conclusion

In this paper, a multi-material approach is used to improve the performance and the compactness of a metamaterial architecture already exhibiting interesting properties in terms of wideness of the bandgap and low frequency cut-off. The proposed unit cell is engineered by joining two different materials, i.e. plastic and steel. This choice makes it possible to obtain a compact design of a low-pass filter and a great design flexibility in terms of bandgap frequency range. In particular, by comparing the present results with the ones achieved in [82] through a single-material counterpart, we reduced the unit cell size from 4 cm to 3 cm and we lowered the opening frequency from 1478.1 Hz to 1257.2 Hz. A metastructure prototype has been realized by manufacturing the unit cell components by means of the SLS and the BDM processes for the plastic skeleton and the metal tetrahedral masses, respectively. The final $1 \times 1 \times 3$ prototype is obtained by manual assembly. The attenuation performances of more than two orders of magnitude has been numerically and experimentally demonstrated. The metastructure, given its dynamic and structural characteristics, can be integrated in a hand-held vibration probe [87], as experimentally demonstrated in this work.

CRediT authorship contribution statement

A. Annessi: Writing – original draft, Visualization, Methodology, Investigation, Formal analysis, Data curation, Conceptualization. **V. Zega:** Writing – review & editing, Validation, Methodology. **P. Chiariotti:** Writing – review & editing, Validation, Methodology. **M. Martarelli:** Writing – review & editing, Validation, Supervision, Project administration, Methodology, Funding acquisition, Conceptualization. **P. Castellini:** Writing – review & editing, Resources, Project administration, Conceptualization.

Funding

Project Proof of Concept "Metablock" C38H23000600002, patent n.102022000015228, funded by the European Union with NextGenerationEU resources (PNRR - Missione 1 "Digitalizzazione, innovazione competitività, cultura e turismo" - Componente 2 "Digitalizzazione, innovazione e competitività nel sistema produttivo" – Investimento 6 "Sistema della proprietà industriale") under the Enhancement Programme VALUE "VALorizzare gli esiti della ricerca UnivErsitaria" of Università Politecnica delle Marche.

Declaration of competing interest

The authors declare the following financial interests/personal relationships which may be considered as potential competing interests: Alessandro Annessi has patent#102022000015228 issued to Università Politecnica delle Marche, Politecnico di Milano. Valentina Zega has patent #102022000015228 issued to Universitá Politecnica delle Marche, Politecnico di Milano. Paolo Chiariotti has patent #102022000015228 issued to Università Politecnica delle Marche, Politecnico di Milano. Milena Martarelli has patent #102022000015228 issued to Universitá Politecnica delle Marche, Politecnico di Milano. Paolo Castellini has patent #102022000015228 issued to Universitá Politecnica delle Marche, Politecnico di Milano. If there are other authors, they declare that they have no known competing financial interests or personal relationships that could have appeared to influence the work reported in this paper.

Data availability

Data will be made available on request.

References

[1] R. Kumar, M. Kumar, J.S. Chohan, S. Kumar, Overview on metamaterial: History, types and applications, Mater. Today: Proc. 56 (2022) 3016–3024, http://dx.doi.org/10.1016/j.matpr.2021.11.423.

[2] S. Brûlé, S. Enoch, S. Guenneau, Emergence of seismic metamaterials: Current state and future perspectives, Phys. Lett. A 384 (1) (2020) 126034, http://dx.doi.org/10.1016/j.physleta.2019.126034.

[3] K. Wang, J. Zhou, D. Tan, Z. Li, Q. Lin, D. Xu, A brief review of metamaterials for opening low-frequency band gaps, Appl. Math. Mech. 43 (7) (2022) 1125–1144, http://dx.doi.org/10.1007/s10483-022-2870-9.

[4] H. Zheng, L. Miao, P. Xiao, K. Lei, Q. Wang, Novel metamaterial foundation with multi low-frequency bandgaps for isolating earthquakes and train vibrations, Structures 61 (2024) 106070, http://dx.doi.org/10.1016/j.istruc.2024.106070.

[5] R. Ardito, C. Comi, V. Zega, A. Corigliano, Metamaterials and MEMS (MetaMEMS): a promising trend in microsystems technology, in: 2023 24th International Conference on Thermal, Mechanical and Multi-Physics Simulation and Experiments in Microelectronics and Microsystems, EuroSimE, IEEE, 2023, http://dx.doi.org/10.1109/eurosime56861.2023.10100824.

[6] Z. Yao, V. Zega, Y. Su, Y. Zhou, J. Ren, J. Zhang, A. Corigliano, Design, fabrication and experimental validation of a metaplate for vibration isolation in MEMS, J. Microelectromech. Syst. 29 (5) (2020) 1401–1410, http://dx.doi.org/10.1109/jmems.2020.3016179.

[7] Z. Yao, V. Zega, Y. Su, Y. Zhou, J. Ren, J. Zhang, A. Corigliano, Design, fabrication and experimental validation of a metaplate for vibration isolation in MEMS, J. Microelectromech. Syst. 29 (2020) 1401–1410.

[8] S. Wang, L. Popa, D. Weinstein, Gan MEMS resonator using a folded phononic crystal structure, Solid State Sens. Actuators Microsyst. Work. Hilton Head Isl. South Carol. 29 (2014) 72–75, URL https://doi.org/10.31438/TRF.HH2014.19.

[9] L. Wang, Y. Liu, P. Du, T. Jiang, F. Ma, A tai chi acoustic metamaterial for low-dimensional joint compressive sensing and simultaneously azimuth-distance location, Mech. Syst. Signal Process. 224 (2025) 112228, http://dx.doi.org/10.1016/j.ymssp.2024.112228, URL https://www.sciencedirect.com/science/article/pii/S0888327024011270.

[10] R. Yu, S. Rui, X. Wang, F. Ma, An integrated load-bearing and vibration-isolation supporter with decorated metamaterial absorbers, Int. J. Mech. Sci. 253 (2023) 108406, http://dx.doi.org/10.1016/j.ijmecsci.2023.108406.

[11] L. Sangiuliano, B. Reff, J. Palandri, F. Wolf-Monheim, B. Pluymers, E. Deckers, W. Desmet, C. Claeys, Low frequency tyre noise mitigation in a vehicle using metal 3D printed resonant metamaterials, Mech. Syst. Signal Process. 179 (2022) 109335, http://dx.doi.org/10.1016/j.ymssp.2022.109335.

[12] M. Nakayama, Acoustic metamaterials based on polymer sheets: from material design to applications as sound insulators and vibration dampers, Polym. J. (2023) http://dx.doi.org/10.1038/s41428-023-00842-0.

[13] Y. Liu, X. An, H. Chen, H. Fan, Vibration attenuation of finite-size metaconcrete: Mechanism, prediction and verification, Compos. Part A: Appl. Sci. Manuf. 143 (2021) 106294, http://dx.doi.org/10.1016/j.compositesa.2021.106294, URL https://www.sciencedirect.com/science/article/pii/S1359835X21000245.

[14] S.J. Mitchell, A. Pandolfi, M. Ortiz, Investigation of elastic wave transmission in a metaconcrete slab, Mech. Mater. 91 (2015) 295–303, http://dx.doi.org/10.1016/j.mechmat.2015.08.004, URL https://www.sciencedirect.com/science/article/pii/S0167663615001726.

[15] F. Mir, M. Saadatzi, R.U. Ahmed, S. Banerjee, Acoustoelastic MetaWall noise barriers for industrial application with simultaneous energy harvesting capability, Appl. Acoust. 139 (2018) 282–292, http://dx.doi.org/10.1016/j.apacoust.2018.04.029.

[16] Muhammad, C.W. Lim, N.S. Vyas, A novel application of multi-resonant dissipative elastic metahousing for bearings, Acta Mech. Solida Sin. 34 (4) (2021) 449–465, http://dx.doi.org/10.1007/s10338-021-00221-3.

[17] W. Liu, L. Wu, J. Sun, J. Zhou, Tunable multifunctional metamaterial sandwich panel with quasi-zero stiffness lattice cores: Load-bearing, energy absorption, and vibration isolation, Adv. Mater. Technol. 9 (4) (2023-12) http://dx.doi.org/10.1002/admt.202301586.

[18] Z. Mei, T. Shi, Y. Lyu, X. Li, X. Cheng, J. Yang, Reconfigurable modular acoustic metamaterial for broadband sound absorption, Mech. Syst. Signal Process. 226 (2025) 112348, http://dx.doi.org/10.1016/j.ymssp.2025.112348, URL https://www.sciencedirect.com/science/article/pii/S0888327025000494.

[19] Z. Yang, H.M. Dai, N.H. Chan, G.C. Ma, P. Sheng, Acoustic metamaterial panels for sound attenuation in the 50–1000 Hz regime, Appl. Phys. Lett. 96 (4) (2010) 041906, http://dx.doi.org/10.1063/1.3299007.

[20] J.-H. He, H.-H. Huang, Complete vibrational bandgap in thin elastic metamaterial plates with periodically slot-embedded local resonators, Arch. Appl. Mech. 88 (8) (2018) 1263–1274, http://dx.doi.org/10.1007/s00419-018-1371-0, URL https://doi.org/10.1007/s00419-018-1371-0.

[21] Y. Song, J. Wen, H. Tian, X. Lu, Z. Li, L. Feng, Vibration and sound properties of metamaterial sandwich panels with periodically attached resonators: Simulation and experiment study, J. Sound Vib. 489 (2020) 115644, http://dx.doi.org/10.1016/j.jsv.2020.115644, URL https://www.sciencedirect.com/science/article/pii/S0022460X20304740.

[22] H. Zhang, S. Chen, Z. Liu, Y. Song, Y. Xiao, Light-weight large-scale tunable metamaterial panel for low-frequency sound insulation, Appl. Phys. Express 13 (6) (2020) 067003, http://dx.doi.org/10.35848/1882-0786/ab916b.

[23] Q. Wang, J. Li, Y. Zhang, Y. Xue, F. Li, Bandgap properties in metamaterial sandwich plate with periodically embedded plate-type resonators, Mech. Syst. Signal Process. 151 (2021) 107375, http://dx.doi.org/10.1016/j.ymssp.2020.107375.

[24] W. Chen, Y.X. Hao, W. Zhang, S.W. Yang, Y.T. Cao, Vibration isolation performance of a novel metamaterials sandwich cylindrical panel by locally resonant band gap, J. Vib. Eng. Technol. (2024) http://dx.doi.org/10.1007/s42417-023-01242-7.

[25] A. Sridhar, V.G. Kouznetsova, M.G.D. Geers, Homogenization of locally resonant acoustic metamaterials towards an emergent enriched continuum, Comput. Mech. 57 (2016) 423–435, http://dx.doi.org/10.1007/s00466-015-1254-y.

[26] Q. Jia, J. Zhang, C. Wang, J. Wen, D. Yu, A macroscopic non-locality homogenization method for predicting static and dynamic behaviors of mechanical metamaterials, Mech. Syst. Signal Process. 235 (2025) 112886, http://dx.doi.org/10.1016/j.ymssp.2025.112886, URL https://www.sciencedirect.com/science/article/pii/S0888327025005874.

[27] G. Yan, Y. Li, S. Yao, G. Yin, X. Huang, Systematic topology optimization of elastic metamaterials for broadband bandgaps and customized mechanical properties, Mech. Syst. Signal Process. 211 (2024) 111260, http://dx.doi.org/10.1016/j.ymssp.2024.111260.

[28] R. Zheng, B. Yi, Y. Tao, X. Peng, Topology optimization of extreme mechanical metamaterials considering the anisotropy of additive manufactured parts, Smart Mater. Struct. 33 (11) (2024) 115024, http://dx.doi.org/10.1088/1361-665x/ad8325.

[29] F. Feng, L. Diao, C. He, M. Tao, Topology optimization of multi-material acoustic metamaterials for low-frequency and broadband sound absorption, Mater. Des. 254 (2025) 114136, http://dx.doi.org/10.1016/j.matdes.2025.114136.

[30] Z. Zhang, J. Yao, F. Scarpa, J. Gao, Shape-functional fusion metamaterials for vibration isolation by integrating forward and reverse deep leaning-driven design, Mech. Syst. Signal Process. 232 (2025) 112739, http://dx.doi.org/10.1016/j.ymssp.2025.112739, URL https://www.sciencedirect.com/science/article/pii/S0888327025004406.

[31] J. Yan, Y. Li, G. Yin, S. Yao, Y. Peng, Inverse design on customised absorption of acoustic metamaterials with high degrees of freedom by deep learning, Mech. Syst. Signal Process. 237 (2025) 112989, http://dx.doi.org/10.1016/j.ymssp.2025.112989, URL https://www.sciencedirect.com/science/article/pii/S0888327025006909.

[32] C.S. Ha, D. Yao, Z. Xu, C. Liu, H. Liu, D. Elkins, M. Kile, V. Deshpande, Z. Kong, M. Bauchy, X. Zheng, Rapid inverse design of metamaterials based on prescribed mechanical behavior through machine learning, Nat. Commun. 14 (1) (2023) http://dx.doi.org/10.1038/s41467-023-40854-1.

[33] J.-H. Bastek, D.M. Kochmann, Inverse design of nonlinear mechanical metamaterials via video denoising diffusion models, Nat. Mach. Intell. 5 (12) (2023) 1466–1475, http://dx.doi.org/10.1038/s42256-023-00762-x.

[34] E. Panahi, A. Hosseinkhani, A. Frangi, D. Younesian, V. Zega, A novel low-frequency multi-bandgaps metaplate: Genetic algorithm based optimization and experimental validation, Mech. Syst. Signal Process. 181 (2022) 109495, http://dx.doi.org/10.1016/j.ymssp.2022.109495, URL https://www.sciencedirect.com/science/article/pii/S0888327022006069.

[35] Y. Chen, T. Li, F. Scarpa, L. Wang, Lattice metamaterials with mechanically tunable Poisson's ratio for vibration control, Phys. Rev. Appl. 7 (2) (2017) 024012, http://dx.doi.org/10.1103/physrevapplied.7.024012.

[36] G. Yan, Y. Li, Y. Wang, G. Yin, S. Yao, Tunable bandgap characteristic of various hexagon-type elastic metamaterials for broadband vibration attenuation, Aerosp. Sci. Technol. 145 (2024) 108872, http://dx.doi.org/10.1016/j.ast.2024.108872.

[37] W. Wu, W. Hu, G. Qian, H. Liao, X. Xu, F. Berto, Mechanical design and multifunctional applications of chiral mechanical metamaterials: A review, Mater. Des. 180 (2019) 107950, http://dx.doi.org/10.1016/j.matdes.2019.107950.

[38] P. Zhao, K. Zhang, L. Qi, Z. Deng, 3D chiral mechanical metamaterial for tailored band gap and manipulation of vibration isolation, Mech. Syst. Signal Process. 180 (2022) 109430, http://dx.doi.org/10.1016/j.ymssp.2022.109430.

[39] Z. Guo, D. Zhu, G. Jiang, J. Zheng, Y. Wang, J. Yang, Wave propagation characteristics of controllable gyroscopic chiral metamaterials, Mech. Syst. Signal Process. 233 (2025) 112811, http://dx.doi.org/10.1016/j.ymssp.2025.112811, URL https://www.sciencedirect.com/science/article/pii/S0888327025005126.

[40] E. Panahi, A. Hosseinkhani, M. Khansanami, D. Younesian, M. Ranjbar, Novel cross shape phononic crystals with broadband vibration wave attenuation characteristic: Design, modeling and testing, Thin-Walled Struct. 163 (2021) 107665, URL https://doi.org/10.1016/J.TWS.2021.107665.

[41] F. Yu, Y. Huo, Q. Ding, C. Wang, J. Yao, Z. He, Y. Sun, H. Gao, A. Sun, Structural design and band gap properties of 3D star-shaped single-phase metamaterials, J. Vib. Eng. Technol. (2022) http://dx.doi.org/10.1007/s42417-021-00415-6.

[42] H. Jiang, M. Zhang, Y. Liu, D. Pei, M. Chen, Y. Wang, Band gaps and vibration isolation of a three-dimensional metamaterial with a star structure, Materials 13 (17) (2020) http://dx.doi.org/10.3390/ma13173812, URL https://www.mdpi.com/1996-1944/13/17/3812.

[43] X. Liu, K. Zhang, H. Shi, F. Hong, H. Liu, Z. Deng, Origami-inspired metamaterial with compression–twist coupling effect for low-frequency vibration isolation, Mech. Syst. Signal Process. 208 (2024) 111076, http://dx.doi.org/10.1016/j.ymssp.2023.111076.

[44] R.L. Lincoln, F. Scarpa, V.P. Ting, R.S. Trask, Multifunctional composites: a metamaterial perspective, Multifunct. Mater. 2 (4) (2019) 043001, http://dx.doi.org/10.1088/2399-7532/ab5242.

[45] X. Yuan, M. Chen, Y. Yao, X. Guo, Y. Huang, Z. Peng, B. Xu, B. Lv, R. Tao, S. Duan, H. Liao, K. Yao, Y. Li, H. Lei, X. Chen, G. Hong, D. Fang, Recent progress in the design and fabrication of multifunctional structures based on metamaterials, Curr. Opin. Solid State Mater. Sci. 25 (1) (2021) 100883, http://dx.doi.org/10.1016/j.cossms.2020.100883.

[46] H. Jafari, R. Sedaghati, Tunable multi-metamaterials intergrated with auxiliary magnetorheological resonators, Mater. Res. Express 10 (12) (2023) 126101, http://dx.doi.org/10.1088/2053-1591/ad1079.

[47] Z. Li, W. Gao, N. Kessissoglou, S. Oberst, M.Y. Wang, Z. Luo, Multifunctional mechanical metamaterials with tunable double-negative isotropic properties, Mater. Des. 232 (2023) 112146, http://dx.doi.org/10.1016/j.matdes.2023.112146.

[48] J. Hua, Y. Zhou, C.Q. Chen, Design and analysis of a tunable multistable mechanical metamaterial, Int. J. Mech. Sci. 272 (2024) 109170, http://dx.doi.org/10.1016/j.ijmecsci.2024.109170.

[49] A. Pundir, A. Gupta, S. Nag, Multi-functional programmable active acoustic meta-device: acoustic switch, lens, and barrier, Sci. Rep. 14 (1) (2024) http://dx.doi.org/10.1038/s41598-024-71737-0.

[50] H. Wang, J. Zhao, X. Wang, P. Liu, J. Gong, Y. Huang, Multi-functional metamaterial based on overdamping effect: Design, investigation, optimization, Int. J. Mech. Sci. 286 (2025) 109890, http://dx.doi.org/10.1016/j.ijmecsci.2024.109890.

[51] J. Zhao, G. Zhou, D. Zhang, I. Kovacic, R. Zhu, H. Hu, Integrated design of a lightweight metastructure for broadband vibration isolation, Int. J. Mech. Sci. 244 (2023) 108069, http://dx.doi.org/10.1016/j.ijmecsci.2022.108069.

[52] Z. Liu, X. Zhang, Y. Mao, Y.Y. Zhu, Z. Yang, C.T. Chan, P. Sheng, Locally resonant sonic materials, Science 289 (5485) (2000) 1734–1736, http://dx.doi.org/10.1126/science.289.5485.1734, URL https://science.sciencemag.org/content/289/5485/1734.

[53] C. Claeys, E. Deckers, B. Pluymers, W. Desmet, A lightweight vibro-acoustic metamaterial demonstrator: Numerical and experimental investigation, Mech. Syst. Signal Process. 70–71 (2016) 853–880, http://dx.doi.org/10.1016/j.ymssp.2015.08.029, URL https://www.sciencedirect.com/science/article/pii/S088832701500391X.

[54] M. Nouh, O. Aldraihem, A. Baz, Vibration characteristics of metamaterial beams with periodic local resonances, J. Vib. Acoust. 136 (6) (2014) http://dx.doi.org/10.1115/1.4028453, 061012.

[55] K.H. Matlack, A. Bauhofer, S. Krödel, A. Palermo, C. Daraio, Composite 3D-printed metastructures for low-frequency and broadband vibration absorption, Proc. Natl. Acad. Sci. 113 (30) (2016) 8386–8390, http://dx.doi.org/10.1073/pnas.1600171113, URL https://www.pnas.org/content/113/30/8386.

[56] H. Meng, D. Chronopoulos, A. Fabro, W. Elmadih, I. Maskery, Rainbow metamaterials for broadband multi-frequency vibration attenuation: Numerical analysis and experimental validation, J. Sound Vib. 465 (2020) 115005, http://dx.doi.org/10.1016/j.jsv.2019.115005.

[57] X. An, C. Lai, H. Fan, C. Zhang, 3D acoustic metamaterial-based mechanical metalattice structures for low-frequency and broadband vibration attenuation, Int. J. Solids Struct. 191–192 (2020) 293–306, http://dx.doi.org/10.1016/j.ijsolstr.2020.01.020, URL https://www.sciencedirect.com/science/article/pii/S0020768320300263.

[58] C. Claeys, N.G. Rocha de Melo Filho, L. Van Belle, E. Deckers, W. Desmet, Design and validation of metamaterials for multiple structural stop bands in waveguides, Extrem. Mech. Lett. 12 (2017) 7–22, http://dx.doi.org/10.1016/j.eml.2016.08.005, Frontiers in Mechanical Metamaterials. URL https://www.sciencedirect.com/science/article/pii/S2352431616300578.

[59] M.V. Barnhart, X. Xu, Y. Chen, S. Zhang, J. Song, G. Huang, Experimental demonstration of a dissipative multi-resonator metamaterial for broadband elastic wave attenuation, J. Sound Vib. 438 (2019) 1–12, http://dx.doi.org/10.1016/j.jsv.2018.08.035, URL https://www.sciencedirect.com/science/article/pii/S0022460X1830542X.

[60] B. Zhao, H.R. Thomsen, X. Pu, S. Fang, Z. Lai, B.V. Damme, A. Bergamini, E. Chatzi, A. Colombi, A nonlinear damped metamaterial: Wideband attenuation with nonlinear bandgap and modal dissipation, Mech. Syst. Signal Process. 208 (2024) 111079, http://dx.doi.org/10.1016/j.ymssp.2023.111079.

[61] A. Krushynska, M. Miniaci, F. Bosia, N. Pugno, Coupling local resonance with bragg band gaps in single-phase mechanical metamaterials, Extrem. Mech. Lett. 12 (2017) 30–36, http://dx.doi.org/10.1016/j.eml.2016.10.004, Frontiers in Mechanical Metamaterials. URL https://www.sciencedirect.com/science/article/pii/S2352431616300542.

[62] L. D'Alessandro, A.O. Krushynska, R. Ardito, N.M. Pugno, A. Corigliano, A design strategy to match the band gap of periodic and aperiodic metamaterials, Sci. Rep. 10 (1) (2020) 16403, http://dx.doi.org/10.1038/s41598-020-73299-3.

[63] X. Hou, J. Feng, X. An, X. Yuan, H. Fan, Hybrid rod-plate lattice metamaterial with broadband vibration attenuation, Appl. Acoust. 216 (2024) 109822, http://dx.doi.org/10.1016/j.apacoust.2023.109822.

[64] Y. Bao, Z. Yao, X. Hu, X. Liu, Y. Shan, T. He, Complete bandgap of three-dimensional helical metamaterial tapered rod with power-law radius, Mech. Syst. Signal Process. 211 (2024) 111257, http://dx.doi.org/10.1016/j.ymssp.2024.111257.

[65] J. Yong, Y. Dong, Z. Wan, W. Li, Y. Chen, Collaborative design of static and vibration properties of a novel re-entrant honeycomb metamaterial, Appl. Sci. 14 (4) (2024) 1497, http://dx.doi.org/10.3390/app14041497.

[66] X. Gao, J. Wei, J. Huo, Z. Wan, Y. Li, The vibration isolation design of a re-entrant negative Poisson's ratio metamaterial, Appl. Sci. 13 (16) (2023) 9442, http://dx.doi.org/10.3390/app13169442.

[67] L. Zhang, Z. Bai, Q. Zhang, Y. Jin, Y. Chen, On vibration isolation performance and crashworthiness of a three-dimensional lattice metamaterial, Eng. Struct. 292 (2023) 116510, http://dx.doi.org/10.1016/j.engstruct.2023.116510.
[68] W. Jiang, M. Yin, Q. Liao, L. Xie, G. Yin, Three-dimensional single-phase elastic metamaterial for low-frequency and broadband vibration mitigation, Int. J. Mech. Sci. 190 (2021) 106023, http://dx.doi.org/10.1016/j.ijmecsci.2020.106023.
[69] Muhammad, C.W. Lim, Phononic metastructures with ultrawide low frequency three-dimensional bandgaps as broadband low frequency filter, Sci. Rep. 11 (1) (2021) 7137, http://dx.doi.org/10.1038/s41598-021-86520-8.
[70] X. Fei, L. Jin, X. Zhang, X. Li, M. Lu, Three-dimensional anti-chiral auxetic metamaterial with tunable phononic bandgap, Appl. Phys. Lett. 116 (2) (2020) 021902, http://dx.doi.org/10.1063/1.5132589.
[71] Muhammad, C. Lim, Dissipative multiresonant pillared and trampoline metamaterials with amplified local resonance bandgaps and broadband vibration attenuation, J. Vib. Acoust. 142 (6) (2020) http://dx.doi.org/10.1115/1.4047358.
[72] N. Kumar, S. Pal, Low frequency and wide band gap metamaterial with divergent shaped star units: Numerical and experimental investigations, Appl. Phys. Lett. 115 (25) (2019) 254101, http://dx.doi.org/10.1063/1.5119754.
[73] W. Zhou, Muhammad, W. Chen, Z. Chen, C. Lim, Actively controllable flexural wave band gaps in beam-type acoustic metamaterials with shunted piezoelectric patches, Eur. J. Mech. A Solids 77 (2019) 103807, http://dx.doi.org/10.1016/j.euromechsol.2019.103807.
[74] W. Elmadih, D. Chronopoulos, W.P. Syam, I. Maskery, H. Meng, R.K. Leach, Three-dimensional resonating metamaterials for low-frequency vibration attenuation, Sci. Rep. 9 (1) (2020) 11503, http://dx.doi.org/10.1038/s41598-019-47644-0.
[75] Muhammad, C. Lim, J. Reddy, Built-up structural steel sections as seismic metamaterials for surface wave attenuation with low frequency wide bandgap in layered soil medium, Eng. Struct. 188 (2019) 440–451, http://dx.doi.org/10.1016/j.engstruct.2019.03.046.
[76] L. D'Alessandro, R. Ardito, F. Braghin, A. Corigliano, Low frequency 3D ultra-wide vibration attenuation via elastic metamaterial, Sci. Rep. 9 (1) (2019) 8039, URL https://doi.org/10.1038/s41598-019-44507-6.
[77] L. D'Alessandro, V. Zega, R. Ardito, A. Corigliano, 3D auxetic single material periodic structure with ultra-wide tunable bandgap, Sci. Rep. 8 (1) (2018) 2262.
[78] L. D'Alessandro, E. Belloni, R. Ardito, F. Braghin, A. Corigliano, Mechanical low-frequency filter via modes separation in 3D periodic structures, Appl. Phys. Lett. 111 (23) (2017) 231902, http://dx.doi.org/10.1063/1.4995554.
[79] Y. Lu, Y. Yang, J.K. Guest, A. Srivastava, 3-d phononic crystals with ultra-wide band gaps, Sci. Rep. 7 (1) (2017) 7137, http://dx.doi.org/10.1038/srep43407.
[80] L. D'Alessandro, E. Belloni, R. Ardito, A. Corigliano, F. Braghin, Modeling and experimental verification of an ultra-wide bandgap in 3D phononic crystal, Appl. Phys. Lett. 109 (22) (2016) 221907, http://dx.doi.org/10.1063/1.4971290.
[81] G. Acar, C. Yilmaz, Experimental and numerical evidence for the existence of wide and deep phononic gaps induced by inertial amplification in two-dimensional solid structures, J. Sound Vib. 332 (24) (2013) 6389–6404, http://dx.doi.org/10.1016/j.jsv.2013.06.022.
[82] A. Annessi, V. Zega, P. Chiariotti, M. Martarelli, P. Castellini, An innovative wide and low-frequency bandgap metastructure for vibration isolation, J. Appl. Phys. 132 (8) (2022) 084903, http://dx.doi.org/10.1063/5.0102410.
[83] W. Setyawan, S. Curtarolo, High-throughput electronic band structure calculations: Challenges and tools, Comput. Mater. Sci. 49 (2) (2010) 299–312, http://dx.doi.org/10.1016/j.commatsci.2010.05.010, URL https://www.sciencedirect.com/science/article/pii/S0927025610002697.
[84] A. Annessi, V. Zega, P. Chiariotti, M. Martarelli, P. Castellini, Static and dynamic characterization of a vibration decoupling element based on a metamaterial structure, in: Model Validation and Uncertainty Quantification, Volume 3, Springer Nature Switzerland, 2023, pp. 45–55, http://dx.doi.org/10.1007/978-3-031-37003-8_8.
[85] PCB model 352C23 datasheet. URL http://www.pcb.com/products?m=352c23.
[86] E. de Barros, C. dÁndrade Souto, Evaluation of a vibration text fixture, Int. J. Acoust. Vib. 22 (3) (2017) http://dx.doi.org/10.20855/ijav.2017.22.3480.
[87] P. Chiariotti, V. Zega, A. Annessi, M. Martarelli, P. Castellini, Patent application file n. 102022000015228. Metastruttura con proprietà isolanti da vibrazioni, 2022.